Reac Kinet Mech Cat (2016) 118:605–619
DOI 10.1007/s11144-016-1011-z

Catalytic oxidation of toluene over active MnO_x catalyst prepared via an alkali-promoted redox precipitation method

Lei Wang[1,2] · Chuanhui Zhang[2] · He Huang[2] · Xuebing Li[2] · Wei Zhang[1] · Mohong Lu[1] · Mingshi Li[1]

Received: 29 December 2015 / Accepted: 23 February 2016 / Published online: 4 March 2016

Abstract MnO_x catalysts were contrastively prepared by an alkali-promoted redox precipitation strategy (MnO_x-RP) and a conventional citrate sol–gel method (MnO_x-SG), and tested for the catalytic oxidation of toluene, where MnO_x-RP exhibited higher catalytic activity, excellent catalytic durability under dry conditions and good regeneration ability under humid conditions. The characterizations results indicated that different crystalline phases but similar textual properties (specific surface area, porosity and morphology) were observed over MnO_x-RP and MnO_x-SG catalysts, while MnO_x-RP presented significantly higher low-temperature reducibility and average oxidation state of Mn as well as higher abundance of surface adsorbed oxygen species compared with MnO_x-SG, thus beneficially resulting in its superior catalytic activity in the reaction.

Keywords VOCs · MnO_x · Redox precipitation · Reducibility · Average oxidation state

Introduction

Volatile organic compounds (VOCs, e.g., alkanes, aromatics, alkene, halogen hydrocarbons, esters, aldehydes, ketones and other) emitted from automobile exhaust and industrial emissions are regarded as one of the main atmospheric pollutants, which lead to serious environmental problems and harmful effect on

✉ Mingshi Li
mingshili@cczu.edu.cn

[1] Jiangsu Key Laboratory of Advanced Catalytic Materials and Technology, School of Petrochemical Engineering, Changzhou University, Changzhou 213164, People's Republic of China

[2] Key Laboratory of Biofuels, Qingdao Institute of Bioenergy and Bioprocess Technology, Chinese Academy of Sciences, Qingdao 266101, People's Republic of China

human physical health [1]. For example, the released VOCs in the atmosphere have been reported to be the precursors for the formation of photochemical smog [2], and many VOCs are proved to be highly carcinogenic and inductively mutational.

During the past decades, a number of oxidative decomposition technologies including catalytic oxidation, ozone-assisted plasma oxidation and photocatalytic oxidation have been developed for VOCs abatement [3]. Among all, catalytic oxidation is recognized as the most effective one because of its advantages such as energy saving, high purification efficiency and the absence of secondary pollution [4]. Previous research has reported that supported precious metals (Au, Pd, Pt and Ru et al.) [5–7], transition metal oxides (MnO_x, Co_3O_4, FeO_x and CuO) [8–11] and perovskite-type metal oxides [12, 13] were widely used as catalysts for the catalytic oxidation of various VOCs. Precious metal catalysts are of high activity and efficiency for VOCs combustion, the expensive cost is the main defect to limit their widespread applications [14, 15]. Thus, it is urgently necessary to search other cheap, green and active catalytic materials as alternatives in present studies [16].

Manganese oxide (MnO_x), as one of the most promising transition metal oxides, has attracted extensive attention because of its excellent redox ability, multiple crystalline phases and valance states as well as environmentally friendly property [9, 17–21]. It has been reported that various manganese oxides such as MnO_2 [22], Mn_2O_3 [23] and Mn_3O_4 [24] exhibit relatively high catalytic activity of VOC oxidation. Recently, Kim et al. [21] reported that the catalytic activity for toluene oxidation varied depending on the manganese oxidation state with a descending sequence of $Mn_3O_4 > Mn_2O_3 > MnO_2$. Shi et al. [25] found that the crystal phases and morphologies of MnO_2 also made significant influence on the toluene oxidation activity, where the MnO_2 with unique structure namely α-MnO_2, ε-MnO_2 and β-MnO_2 presented higher catalytic activity than the amorphous MnO_2 following a sequence of α-MnO_2 > ε-MnO_2 > β-MnO_2 > amorphous-MnO_2. Additionally, it is well accepted that the crystalline structure, valence distribution and morphological properties of MnO_x materials are closely related to the preparation methods. The modification and optimization of material synthesis strategy not only result in the achievement of oriented control on the physicochemical properties, but also remarkable enhancement in the catalytic performances of these catalysts in the reaction. From this viewpoint, it remains of great significance to make further improvement on the preparation strategy in order to obtain highly active MnO_x catalyst for VOC oxidation.

In this work, we report an alkali-promoted redox precipitation method to synthesize MnO_x oxide at room temperature and atmospheric pressure. For a comparison, the traditional citrate sol–gel (SG) method was also applied to prepare different MnO_x catalyst. Their catalytic performances for VOC elimination were evaluated in the reaction of toluene oxidation, and their physicochemical properties were characterized by numerous techniques including X-ray diffraction (XRD), scanning electron microscopy (SEM), N_2 adsorption–desorption isotherms, hydrogen temperature-programmed reduction (H_2-TPR) and X-ray photoelectron spectroscopy (XPS) in order to clarify the structure–reactivity relationship.

Experimental

Catalysts preparation

The MnO_x catalyst was prepared by an alkali-promoted redox precipitation route. Typically, $KMnO_4$ (0.01 mol, Aladdin, AR) and $Mn(NO_3)_2$ (0.015 mol, Aladdin, 50 wt% aqueous solution) as manganese precursors were mixed with a complete dissolution by deionized water, and subsequently 2 mol L^{-1} NaOH aqueous solution as the alkali precipitant was added under magnetic stirring at room temperature until the pH reached 10. After aging at room temperature for 4 h, the suspension was filtered, and thoroughly washed with deionized water. The collected precipitate was dried at 120 °C in an electric oven overnight and followed by the calcination at 400 °C for 4 h in a muffle furnace under air atmosphere.

In addition, MnO_x catalyst was also prepared by means of a citrate sol–gel method in order to investigate the effect of synthesis methods. Typically, certain amounts of citric acid (0.03 mol, Aladdin, AR) were added into the diluted $Mn(NO_3)_2$ (0.02 mol, Aladdin, 50 wt% aqueous solution) aqueous solution at room temperature. After heating at 80 °C for 5 h to evaporate the excess amount of water under magnetic stirring, the formed viscous gel was dried at 120 °C overnight. The resulting material was thermally pretreated at 200 °C for 4 h (the heating rate of 2 °C min^{-1}) and further calcined at 400 °C for 4 h in a muffle furnace under air atmosphere.

For simplifying the description below, the prepared MnO_x catalysts above were denoted as MnO_x-RP and MnO_x-SG.

Catalyst characterizations

Powder X-ray diffraction (XRD) patterns were recorded on a Bruker D8 Advance diffractometer with Cu K_α radiation ($\lambda = 1.5406$ Å) in the range of 20–80° with a step size of 0.05°. The diffraction peaks of the crystalline phases were analyzed compared with those standard powder diffraction files in the Joint Committee on Powder Diffraction Standards Database (JCPDS PDF 2000, International Centre of Diffraction Data, Pennsylvania). N_2 adsorption–desorption isotherms were measured on a Micrometrics ASAP 2010C adsorption analyzer at −196 °C. Prior to the measurements, all samples were degassed in a vacuum at 200 °C for 3 h. The specific surface area (SSA) was calculated by Brunauer–Emmett–Teller (BET) method, and the pore volume and pore size were determined by Barrett–Joyner–Halenda (BJH) method from the desorption branch of the isotherms. Scanning electron microscopy (SEM) was taken on a Zeiss SUPRA-55 field emission scanning electron microscope at 5 kV. Hydrogen temperature-programmed reduction (H_2-TPR) was carried out on a self-designed setup equipped with a Hidden QIC-20 mass spectrometer (MS) as the detector. Typically, 100 mg of the catalyst (60-80 mesh) was pretreated at 300 °C for 0.5 h in a helium stream (25 mL min^{-1}). After cooling down to 60 °C under the same atmosphere, hydrogen reduction was conducted in a 5 vol% H_2/He stream (30 mL min^{-1}) in the range of 60–600 °C at a

ramp of 10 °C min^{-1}, and the signal of consumed hydrogen was collected by the MS detector. X-ray photoelectron spectroscopy (XPS) analysis was performed on a Thermo VG ESCALAB250 spectrometer with Al K_α radiation (1486.6 eV). The binding energy (BE) was determined by utilizing C 1s of adventitious carbon (284.6 eV) as a reference. XPS spectra were deconvoluted by the curve fitting with the XPS Peak software.

Catalytic testing

The catalytic oxidation of toluene was conducted in a continuous flow fixed-bed tubular quartz reactor (I.D. = 7 mm) under atmospheric pressure. 0.4 g of the catalyst (60–80 mesh) deposited on a quartz wool-plug was loaded in the middle of the reactor with the reaction temperature continuously monitored by a K-type thermocouple within a concentric thermowell. The gas feed with the total flow rate of 100 mL min^{-1} consisted of 1000 ppm toluene and air, corresponding to a weight hourly space velocity (WHSV) of 15,000 mL g^{-1} h^{-1}. The toluene vapor was generated by bubbling air (14 mL min^{-1}) through the toluene container chilled in an ice-water isothermal bath. Prior to each experiment, the reactor was heated from room temperature to 100 °C and maintained for 1 h at this temperature to avoid

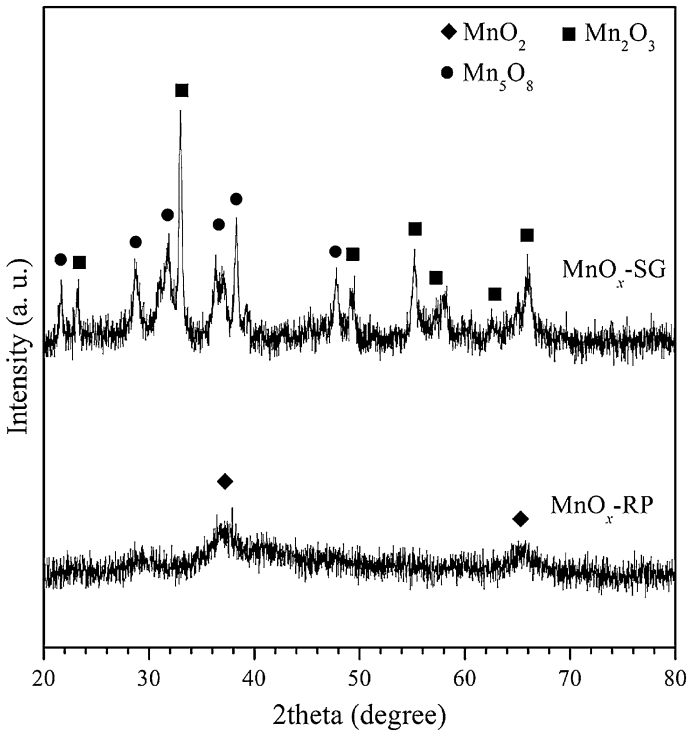

Fig. 1 XRD patterns of prepared MnO_x catalysts

over-estimation of toluene conversion, and then continuously raised up to 300 °C. The toluene conversion at independent reaction temperature was obtained in a steady state after it was maintained for 45 min. Toluene and possible organic products were analyzed by an online Agilent 7890A gas chromatograph with a flame ionization detector (FID). The toluene conversion (X %) was calculated based on the following equation:

$$X\% = \frac{[C_7H_8]_{in} - [C_7H_8]_{out}}{[C_7H_8]_{in}} \times 100$$

Here $[C_7H_8]_{in}$ and $[C_7H_8]_{out}$ denoted the inlet and outlet concentrations of toluene, respectively.

Results and discussion

Material characterizations

The XRD patterns of MnO_x-RP and MnO_x-SG are illustrated in Fig. 1. It can be observed that all diffraction peaks identified in the patterns corresponded to characteristic features of MnO_x phases. In particular, the diffraction patterns of MnO_x-SG could be indexed as a mixture of bixbyite Mn_2O_3 (JCPDS No. 41-1442) and monoclinic Mn_5O_8 (JCPDS No. 39-1218), while MnO_x-RP presented the typical peaks assignable to an amorphous MnO_2 (JCPDS No. 44-0992). The differences in the XRD patterns of MnO_x-RP and MnO_x-SG catalysts revealed that the crystalline structures and phases of manganese oxides were strongly dependent on the

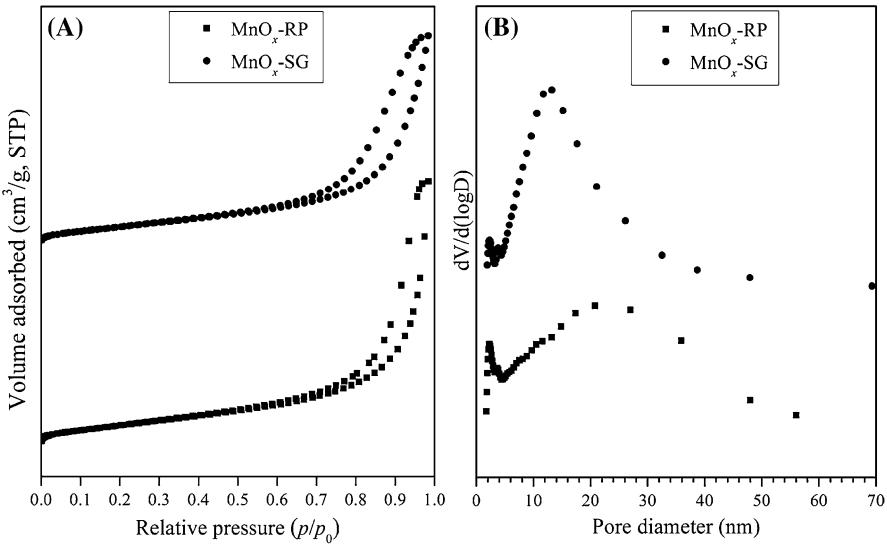

Fig. 2 **A** N_2 adsorption–desorption isotherms and **B** pore-size distributions of prepared MnO_x catalysts

preparation methods and conditions. It can be deduced that the addition of the alkali solution favored the formation of MnO_2 precipitate and/or precursor in the redox-precipitation process, while the relatively low calcination temperature with limited heat release resulting from the combustion of organic fuel (citric acid) would be suitable for the formation of Mn_2O_3 and Mn_5O_8 [26].

The nitrogen adsorption–desorption isotherms and the pore size distributions of MnO_x-RP and MnO_x-SG catalysts are illustrated in Figs. 2A and 2B, respectively, and the specific surface area and pore volume of each catalyst are summarized in Table 1. As shown in Fig. 2A, both of MnO_x catalysts exhibited type IV isotherms with H3 hysteresis loops in terms of the IUPAC classifications, which principally corresponded to the presence of mesoporous structures on the catalysts [27–29]. Additionally, the formation of mesoporous materials can be substantiated by the pore size distributions in Fig. 2B, where the pore size of MnO_x-RP and MnO_x-SG was mainly distributed in the range of 10–30 and 5–25 nm, respectively. As indicated in Table 1, MnO_x-RP possessed higher specific surface area and pore volume with the values of 36 $m^2\ g^{-1}$ and 0.13 $cm^3\ g^{-1}$, respectively, in comparison with MnO_x-SG.

The SEM images of the prepared MnO_x catalysts are shown in Fig. 3. It can be observed that no special morphology but similar amorphous agglomerates of nanoparticles were obtained over MnO_x-RP and MnO_x-SG catalysts. Besides, the MnO_x particles presented irregular size dimensions and shapes with obvious angular on the surface, indicating the formation of unordered and random structures through the present preparation methods.

The relative reducibility of prepared MnO_x catalysts was investigated by H_2-TPR measurements and their TPR profiles are illustrated in Fig. 4. Both catalysts showed the presence of mainly two reduction components in the low and high temperature regions. For the MnO_x-RP catalyst, there was an intense peak centered at 287 °C with two other small shoulder peaks around 160 and 220 °C in the low-temperature region, which could be attributed to the reduction of surface adsorbed oxygen species as well as MnO_2 into Mn_2O_3 or Mn_3O_4 [30–32], while the peak centered at 413 °C in the high-temperature region was possibly due to the further reduction of Mn_2O_3 and/or Mn_3O_4 into MnO. Comparatively for the MnO_x-SG catalyst, the broad peak centered at 320 °C with several shoulder uptakes around 220 and 270 °C

Table 1 Physicochemical properties of all prepared MnO_x catalysts

Catalysts	SSA[a] ($m^2\ g^{-1}$)	Pore volume[b] ($cm^3\ g^{-1}$)	Crystalline phases[c]	Surface atomic ratios[d] (%)		AOS of Mn[d]	O_{ads}/O^d_{latt}
				Mn	O		
MnO_x-RP	36	0.13	MnO_2	0.24	0.76	3.85	0.60
MnO_x-SG	33	0.10	$Mn_2O_3 + Mn_5O_8$	0.27	0.73	3.45	0.56

[a] Determined from the N_2 adsorption–desorption isotherms by BET method

[b] Determined from the N_2 adsorption–desorption isotherms by BJH method

[c] Identified from XRD patterns

[d] Determined from XPS analysis

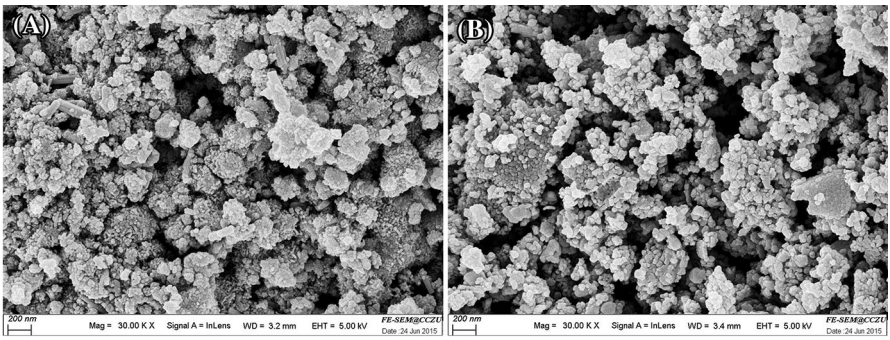

Fig. 3 SEM images of **A** MnO_x-RP and **B** MnO_x-SG

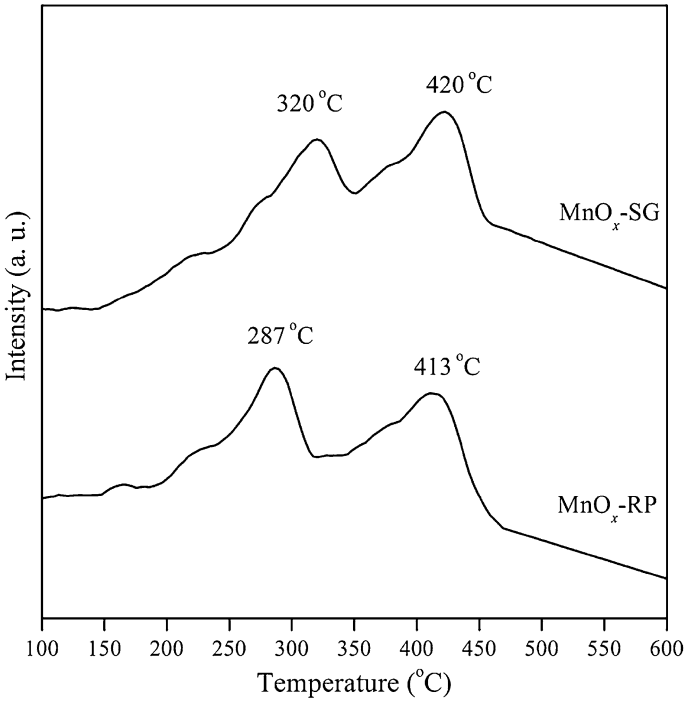

Fig. 4 H_2-TPR profiles of prepared MnO_x catalysts

could be attributed to the reduction of surface oxygen species and Mn_5O_8 into Mn_2O_3 or Mn_3O_4, whereas the subsequent reduction of manganese oxides into MnO resulted in the high-temperature peak at 420 °C [33]. It should be specifically noted that the temperature of reduction peak maximum over MnO_x-RP in the low-temperature region was much lower than that over MnO_x-SG, 287 and 320 °C, respectively. More importantly, MnO_x-RP exhibited more obvious reduction uptakes in the temperature range of below 250 °C compared with MnO_x-SG. All

these observations indicated that the MnO_x-RP catalyst presented even higher low-temperature reducibility than MnO_x-SG.

In order to investigate the surface element compositions, the oxidation states of manganese and the nature of surface oxygen species, the prepared MnO_x catalysts were analyzed by the XPS technique. The surface atomic ratios of Mn and O elements are summarized in Table 1. It can be observed that the atomic ratios of O were much higher than the nominal values (0.30, 0.32 and 0.37 for Mn_2O_3, Mn_5O_8 and MnO_2, respectively) over both of MnO_x-RP and MnO_x-SG catalysts, indicating the enrichment of surface oxygen species possibly due to the presence of moisture, carbonates and other oxygen-containing groups. Additionally, the surface atomic ratio of Mn over MnO_x-RP was a little lower than that over MnO_x-SG, which was in good agreement with their crystalline phases compositions identified by XRD analysis.

Under the consideration that there are minor differences in the binding energies of Mn^{2+}, Mn^{3+} and Mn^{4+} as well as the complexity of various satellites peaks in the Mn 2p spectra, we followed the approach of Galakhov et al. [34] to determine the average oxidation states of Mn over MnO_x-RP and MnO_x-SG catalysts by analyzing their Mn 3s energy regions. As shown in Fig. 5, MnO_x-RP and MnO_x-SG catalysts possessed the splitting values (ΔE_{3s}) of 4.9 and 5.2 eV, respectively. Moreover, it has been previously studied that a linear relationship was present between the average oxidation state of Mn and the splitting values (ΔE_{3s}) of Mn 3 s

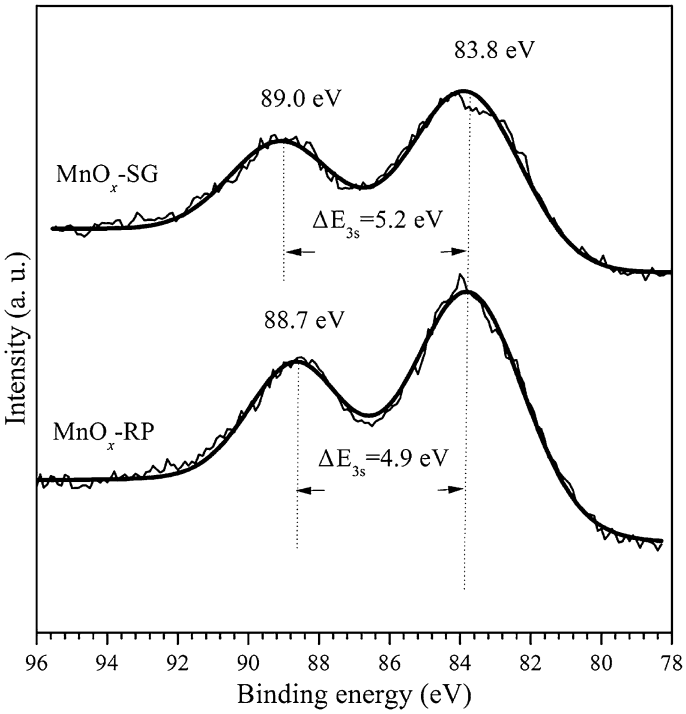

Fig. 5 Mn 3s XPS spectra of prepared MnO_x catalysts

spectra by quantificational measurements of the Mn 3s spectra of those pure MnO_x oxides, namely MnO, Mn_3O_4, Mn_2O_3 and MnO_2 [35]. In Fig. 6, it is clearly indicated that the magnitude of the splitting values from MnO_2 to MnO increased linearly as a function of the manganese valence states. Accordingly, the average oxidation states of Mn over MnO_x-RP and MnO_x-SG were quantitatively determined based on a linear fitting calculation of their ΔE_{3s} values, +3.85 and +3.45, respectively. Clearly, MnO_x-RP exhibited higher average oxidation state of Mn than MnO_x-SG, which was consistent with its amorphous MnO_2 component on the surface.

The O 1s spectra of prepared MnO_x catalysts are shown in Fig. 7. Upon deconvolution, the O 1s spectra showed three peaks at the binding energies of 529.6, 531.5 and 533.3 eV, which corresponded to surface lattice oxygen (O_{latt}), surface adsorbed oxygen species (O_{ads}) and oxygen in surface adsorbed water molecules (O_{wat}), respectively [36–38]. Furthermore, it can be observed that the surface adsorbed oxygen peak (ca. 531.5 eV) of MnO_x-RP catalyst was broader and stronger than that of MnO_x-SG catalyst, suggesting a higher concentration of adsorbed oxygen species on the MnO_x-RP catalyst. Indeed, as illustrated in Table 1, MnO_x-RP exhibited higher O_{ads}/O_{latt} molar ratio than MnO_x-SG, 0.60 and 0.56, respectively, confirming its more abundance of adsorbed oxygen species on the surface.

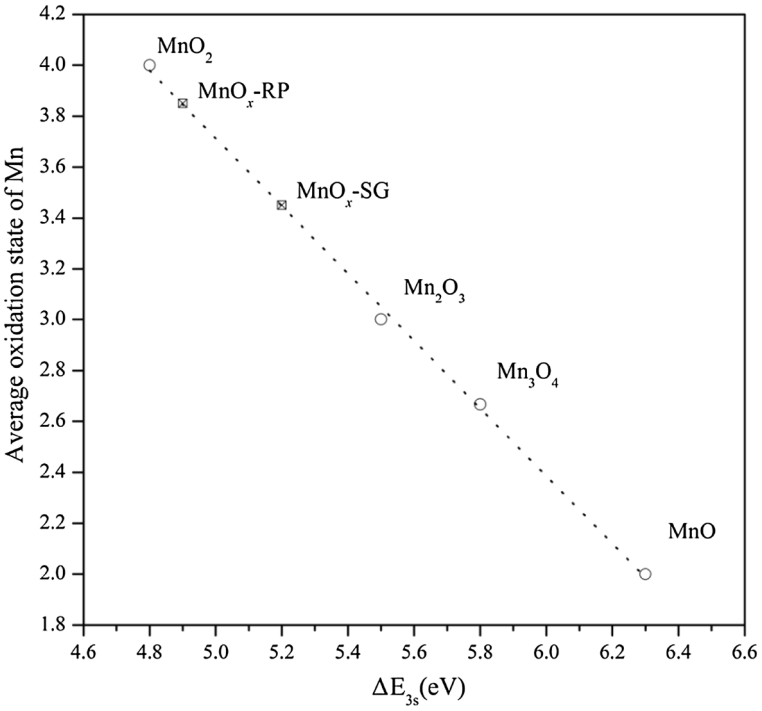

Fig. 6 Relationship of average oxidation state of Mn with the splitting values (ΔE_{3s}) of Mn 3s spectra (linear fitting was indicated with a *dotted line*)

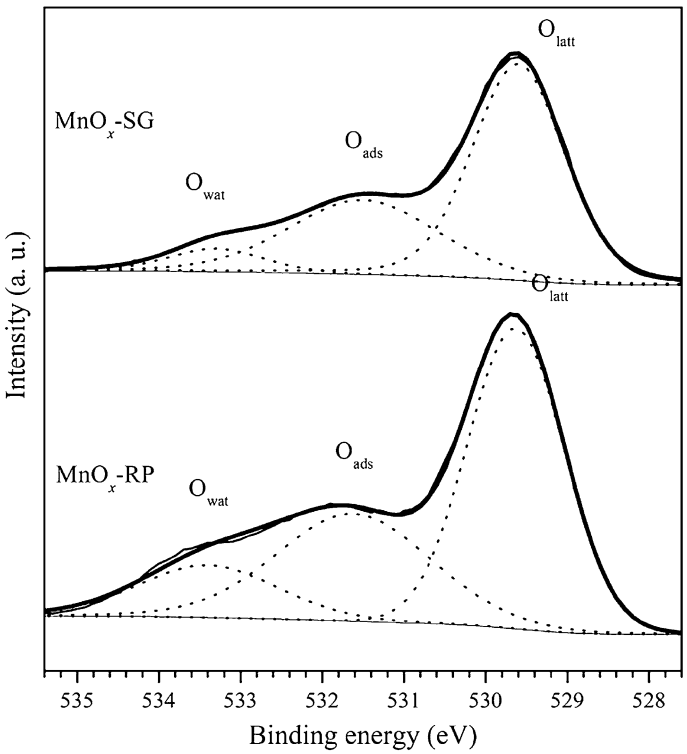

Fig. 7 O1s XPS spectra of prepared MnO_x catalysts (the peaks after XPS spectra deconvolution were indicated with *dotted lines*)

Catalytic performance for toluene oxidation

The catalytic test for toluene oxidation was performed in a light-off process, and the obtained light-off curves as a function of reaction temperature over the prepared MnO_x catalysts are shown in Fig. 8. Prior to the activity evaluation, a blank test was also performed only loaded with quartz wool in the reactor in order to eliminate the homogeneous effect in the reaction. In Fig. 8, it can be demonstrated that no toluene conversion was observed below 300 °C, confirming the absence of homogeneous reaction. For the MnO_x catalysts, MnO_x-RP exhibited much higher catalytic activity with T_{50} (temperature corresponding to 50 % of toluene conversion) and T_{90} (temperature corresponding to 90 % of toluene conversion) of 210 and 230 °C, respectively. MnO_x-SG exhibited lower catalytic activity with T_{50} and T_{90} of 235 and 250 °C. However, complete conversion of toluene can be achieved below 300 °C. These results suggested that MnO_x catalysts, especially MnO_x-RP, presented good catalytic performance in the reaction of toluene oxidation. It is important to note that the final products in the effluent were CO_2 and H_2O without the detection of any incomplete oxidation byproducts, which was confirmed by a good carbon balance of 99.5 % in each catalytic run.

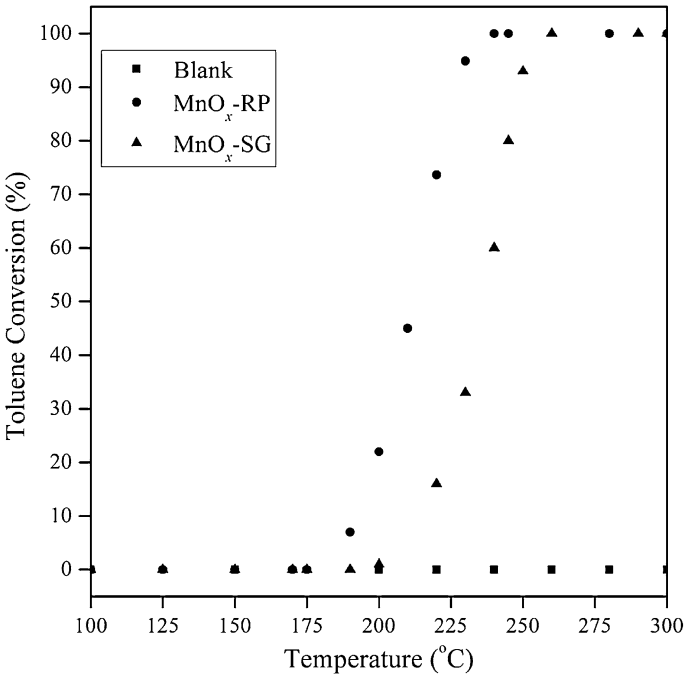

Fig. 8 Light-off curves of toluene oxidation as a function of reaction temperature over prepared MnO_x catalysts. Reaction conditions: 0.4 g catalyst; total flow = 100 mL min^{-1}, 1000 ppm toluene, air balance; WHSV = 15,000 mL g^{-1} h^{-1}

With the aim to evaluate the maintenance of long-term activity, catalytic durability tests for toluene oxidation over MnO_x-RP catalyst were carried out for 60 h at the reaction temperatures of T_{50} and T_{90}, respectively. As shown in Fig. 9, the toluene conversion remained relatively stable without any catalytic deactivation observed during the overall period at 230 and 210 °C, indicating that MnO_x-RP catalyst showed excellent catalytic durability for toluene oxidation under dry conditions.

Considering that an inhibitive action on the catalytic activity of some catalyst is usually induced by the water vapor introduced from the feed stream or produced in the catalytic reaction, it is of great significance to evaluate the catalytic durability of MnO_x catalyst for toluene oxidation under humid conditions. As shown in Fig. 10, complete toluene conversion was always maintained during the first 18 h without the addition of water vapor. However, a gradual decrease in toluene conversion occurred when introducing 1 vol% water vapor into the feed stream, and continuous decrease in toluene conversion was markedly observed with the addition of higher concentration of water (3 vol%) into the feed stream. These results indicated that water vapor made an obvious inhibitive effect on the catalytic activity of MnO_x-RP catalyst because of the competitive adsorption of water and toluene molecules on surface active sites. Afterwards, gradual recovery of catalytic activity was achieved with the operation of reducing water vapor concentration (1 vol%), and complete

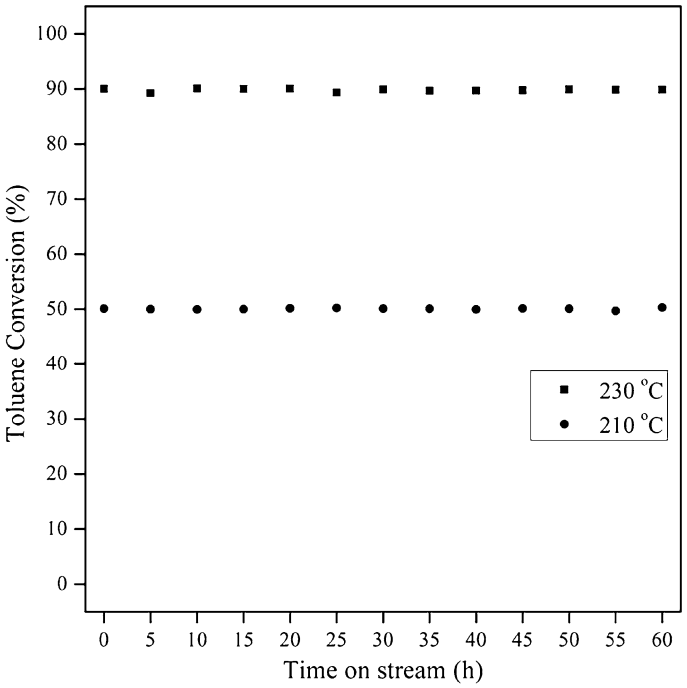

Fig. 9 Toluene conversion as a function of time on stream over MnO_x-RP catalysts at 230 and 210 °C under dry conditions. Reaction conditions: 0.4 g catalyst; total flow = 100 mL min^{-1}, 1000 ppm toluene, air balance; WHSV = 15,000 mL g^{-1} h^{-1}

toluene conversion was obtained after the removal of water vapor, suggesting the good regeneration ability of MnO_x-RP catalyst.

For a comparison, the catalyst activity of MnO_x in this work and those previously reported in the literature for the catalytic oxidation of toluene are summarized in Table 2. It can be clearly observed that the T_{90} value of MnO_x-RP (230 °C) for toluene oxidation was lower than those of the majority of reported catalysts such as 0.5 wt% Pd/$LaMnO_3$ [39] (T_{90} = 250 °C), Mn_3O_4 [21] (T_{90} = 270 °C), AgMn/SBA-15 [40] (T_{90} = 255 °C), $LaMnO_3$ [41] (T_{90} = 249 °C) $La_{0.6}Sr_{0.4}FeO_3$ [42] (T_{90} = 280 °C) and CuO/Mn_2O_3 [43] (T_{90} = 318 °C) under similar reaction conditions, which revealed the outstanding catalytic behavior of the prepared MnO_x catalyst in this study.

Structure–reactivity relationship

Based on the results from catalyst characterization and catalytic testing, a comprehensive discussion was performed to study the correlation between physicochemical properties and catalytic activities. It is well accepted that the specific surface area, structural morphology, low-temperature reducibility, manganese oxidation state as well as oxygen species are important parameters to

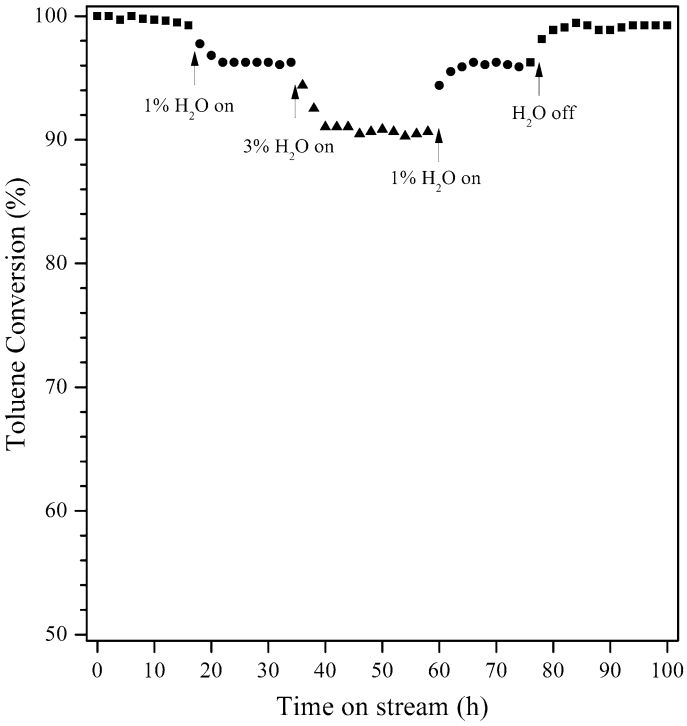

Fig. 10 Toluene conversion as a function of time on stream over MnO_x-RP catalysts at 235 °C under humid conditions. Reaction conditions: 0.4 g catalyst; total flow = 100 mL min^{-1}, 1000 ppm toluene, air balance; WHSV = 15,000 mL g^{-1} h^{-1}

Table 2 Catalytic activities of MnO_x-RP in this work and other catalytic systems previously reported in literatures

Catalysts	WHSV (mL g^{-1} h^{-1})	T_{90}	Reference
0.5 wt%Pd/$LaMnO_3$	18,000	250	[39]
Mn_3O_4	15,000	270	[21]
AgMn/SBA-15	15,000	255	[40]
β-MnO_2	15,000	375	[21]
α-Mn_2O_3	15,000	295	[21]
$LaMnO_3$	20,000	249	[41]
$La_{0.6}Sr_{0.4}FeO_3$	20,000	280	[42]
CuO/Mn_2O_3	12,000	318	[43]
MnO_x-RP	15,000	230	This work

influence the catalytic activity of MnO_x catalysts. In this work, no significant differences on the porous and morphological properties were observed between MnO_x-RP and MnO_x-SG catalysts. Moreover, there was no evident correlation between the specific surface area and the catalytic activity because of their close SSA values. However, as derived from H_2-TPR and XPS analysis, MnO_x-RP

presented higher low-temperature reducibility and average oxidation state of Mn as well as more abundance of surface adsorbed oxygen species, thus resulting in an improved catalytic activity for toluene oxidation in comparison with MnO_x-SG. These observations evidenced that the parameters including low-temperature reducibility, Mn oxidation state and surface adsorbed species would play crucial roles for the catalytic activity of MnO_x materials in the oxidation reactions.

Conclusions

MnO_x catalysts were contrastively prepared by an alkali-promoted redox precipitation strategy and a contrastive citrate sol–gel method, and their catalytic performances were evaluated for the catalytic oxidation of toluene. Catalytic testing results indicated that MnO_x-RP exhibited higher catalytic activity, excellent catalytic durability under dry conditions and good regeneration ability under humid conditions. As derived from characterization results, different crystalline phases but similar textual properties (specific surface area, porosity and morphology) were observed over MnO_x-RP and MnO_x-SG catalysts. However, MnO_x-RP possessed higher low-temperature reducibility and average oxidation state of Mn as well as more abundance of surface adsorbed oxygen species compared with MnO_x-SG, which were the significant factors responsible for its superior catalytic activity in the reaction.

Acknowledgments The financial supports from National Natural Science Foundation of China (Grant No. 21307009, 21276263) are gratefully acknowledged.

References

1. Tidahy HL, Siffert S, Lamonier J-F, Zhilinskaya EA, Aboukais A, Yuan Z-Y, Vantomme A, Su B-L, Canet X, Deweireld G (2006) Appl Catal A 310:61–69
2. Chen HL, Lee HM, Chen SH, Chang MB, Yu SJ, Li ASN (2009) Environ Sci Technol 43:2216–2227
3. Zhou G, Lan H, Wang H, Xie H, Zhang G, Zheng X (2014) J Mol Catal A 393:279–288
4. Zhang C, Liu F, Zhai Y, Ariga H, Yi N, Liu Y, Asakura K, Flytzani-Stephanopoulos M, He H (2012) Angew Chem Int Ed 51:9628–9632
5. Huang H, Leung DYC (2011) ACS Catal 1:348–354
6. Zhang C, He H, Tanaka K (2006) Appl Catal B 65:37–43
7. An N, Zhang W, Yuan X, Pan B, Liu G, Jia M, Yan W, Zhang W (2013) Chem Eng J 215–216:1–6
8. Gomez DM, Galvita VV, Gatica JM, Vidal H, Marin GB (2014) Phys Chem Chem Phys 16:11447–11455
9. Li J, Li L, Cheng W, Wu F, Lu X, Li Z (2014) Chem Eng J 244:59–67
10. Rezaei E, Soltan J (2014) Appl Catal B 148–149:70–79
11. Deng J, Zhang L, Dai H, Xia Y, Jiang H, Zhang H, He H (2010) J Phys Chem C 114:2694–2700
12. Liu Y, Dai H, Du Y, Deng J, Zhang L, Zhao Z, Au CT (2012) J Catal 287:149–160
13. Blasin-Aubé V, Belkouch J, Monceaux L (2003) Appl Catal B 43:175–186
14. Karthik M, Lin L-Y, Bai H (2009) Microporous Mesoporous Mater 117:153–160
15. Zuo S, Zhou R (2008) Microporous Mesoporous Mater 113:472–480
16. Zhang C, Guo Y, Guo Y, Lu G, Boreave A, Retailleau L, Baylet A, Giroir-Fendler A (2014) Appl Catal B 148–149:490–498
17. Brock SL, Duan N, Tian Z, Giraldo O, Zhou H, Suib SL (1998) Chem Mater 10:2619–2628
18. Santos VP, Pereira MFR, Órfão JJM, Figueiredo JL (2009) Top Catal 52:470–481

19. Santos VP, Pereira MFR, Órfão JJM, Figueiredo JL (2010) Appl Catal B 99:353–363
20. Luo J, Zhang Q, Huang A, Suib S (2000) Microporous Mesoporous Mater 35:209–217
21. Kim SC, Shim WG (2010) Appl Catal B 98:180–185
22. Lahousse C, Bernier A, Grange P, Delmon B, Papaefthimiou P, Ioannides T, Verykios X (1998) J Catal 178:214–225
23. Piumetti M, Fino D, Russo N (2015) Appl Catal B 163:277–287
24. Baldi M, Finocchio E, Milella F, Busca G (1998) Appl Catal B 16:43–51
25. Shi F, Wang F, Dai H, Dai J, Deng J, Liu Y, Bai G, Ji K, Au CT (2012) Appl Catal B 433–434:206–213
26. Andreoli S, Deorsola FA, Galletti C, Pirone R (2015) Chem Eng J 278:174–182
27. Leofanti G, Padovan M, Tozzola G, Venturelli B (1998) Catal Today 41:207–219
28. Pawelec B, Parola VL, Navarro RM, Murcia-Mascarós S, Fierro JLG (2006) Carbon 44:84–98
29. Wang X, Zhang X, Wang Y, Liu H, Qiu J, Wang J, Han W, Yeung KL (2011) Chem Mater 23:4469–4479
30. Du Y, Meng Q, Wang J, Yan J, Fan H, Liu Y, Dai H (2012) Microporous Mesoporous Mater 162:199–206
31. Wang X, Kang Q, Li D (2008) Catal Commun 9:2158–2162
32. Garcia T, Sellick D, Varela F, Vázquez I, Dejoz A, Agouram S, Taylor SH, Solsona B (2013) Appl Catal A 450:169–177
33. Mirzaei A (2003) Appl Catal A 253:499–508
34. Galakhov VR, Demeter M, Bartkowski S (2002) Phys Rev B 65:113102
35. Zhang C, Wang C, Hua W, Guo Y, Lu G, Gil S, Giroir-Fendler A (2016) Appl Catal B 186:173–183
36. Fierro JLG, Tejuca LG (1987) Appl Surf Sci 27:453–457
37. Natile MM, Ugel E, Maccato C, Glisenti A (2007) Appl Catal B 72:351–362
38. Kaliaguine S, Neste AV, Szabo V, Gallot JE, Bassir M, Muzychuk R (2001) Appl Catal A 209:345–358
39. Musialik-Piotrowska A, Landmesser H (2008) Catal Today 137:357–361
40. Qu Z, Bu Y, Qin Y, Wang Y, Fu Q (2013) Appl Catal B 132–133:353–362
41. Liu Y, Dai H, Du Y, Deng J, Zhang L, Zhao Z (2012) Appl Catal B 119–120:20–31
42. Zhao Z, Dai H, Deng J, Du Y, Liu Y, Zhang L (2012) Microporous Mesoporous Mater 163:131–139
43. Genuino HC, Dharmarathna S, Njagi EC, Mei MC, Suib SL (2012) J Phys Chem C 116:12066–12078